Energy Reports 8 (2022) 14741–14752

Contents lists available at ScienceDirect

Energy Reports

journal homepage: www.elsevier.com/locate/egyr

Direct-current electrical systems integration on a hybrid skidder using a parallelized step-down power converter array

Matija Krznar, Danijel Pavković *, Mihael Cipek

Faculty of Mechanical Engineering and Naval Architecture, University of Zagreb, Zagreb, Croatia

ARTICLE INFO

Article history:
Received 10 January 2022
Received in revised form 30 September 2022
Accepted 31 October 2022
Available online xxxx

Keywords:
Step-down DC–DC converter
Power distribution system
Hybrid skidder
Efficiency analysis

ABSTRACT

This paper deals with the control of the direct-current to direct-current (DC/DC) energy conversion between high voltage and low voltage systems within a hybrid electric power-train structure intended to be used in articulated forestry tractor, also known as skidder. Electrical part of the hybrid power-train is modeled for the case of utilization of a parallel array of step-down (buck) DC/DC power converters as a bridge between the high and low voltage DC buses. Thus obtained models are used to derive the control laws for the primary-level (power converter voltage/current) control systems, and the secondary level (power allocation) control strategy, which are simulated within the MATLAB/Simulink™ software environment, and subsequently verified by means of laboratory experiments. Final results are also used to gain insights about the efficiency of the DC/DC conversion process and to formulate practical rules for parallelized DC/DC converter operation aimed at maximization of overall DC-to-DC power conversion efficiency.

1. Introduction

With the non-renewable nature of fossil fuel resources and their limited supply (Sorrell et al., 2010), the transportation sector is in dire need of a shift towards alternative energy sources in order to reduce its fossil fuel consumption, currently amounting to about 20% of global fossil fuel uptake (McCollum et al., 2014), thus being the second largest consumer worldwide, and proportionally contributing to carbon-dioxide (CO_2) emissions (Saber and Venayagamoorthy, 2011). Hence, in recent years great emphasis has been placed on hybrid and electric vehicles, given the advantages they bring in reducing fuel consumption and harmful gas emissions, and, thus, preserving the environment (Yong et al., 2015). Since hybrid vehicles use an internal combustion engine (ICE) in conjunction with one or more electrical machines, they represent a good trade-off between the fossil fuel consumption reduction, range and autonomy, and overall vehicle cost (Fuhs, 2009).

On the other hand, hybrid vehicles are a complex mechanical and electrical system, wherein mechanical energy is produced by a conventional ICE-based drive, which needs to be distributed in a controlled manner between individual hybrid electric vehicle powertrain components (Liu, 2017). In hybrid vehicles, the task of electric machines, power electronics systems and battery energy storage is to process and control the transmission of electricity so that the vehicle has sufficient motive power with high overall efficiencies over a wide range of driving modes (Fuhs, 2009). However, depending on the type and configuration of the hybrid vehicle, the cost of electric machines and power electronics may account for nearly 25% of the total material investment cost, which is near the cost of the battery energy storage system (Liu, 2017). Moreover, hybrid electric vehicle powertrain needs to be controlled in a precise manner in order to comply with the driver request while providing good riding comfort (Liu et al., 2021), and also maintaining the battery state-of-charge within prescribed bounds during the hybrid vehicle driving mission (Jing et al., 2021). Since power electronics-based power conversion and its efficiency is one of the most important features of hybrid vehicles, it needs to be carefully investigated in order to optimize the overall hybrid electric power system operation (Williamson et al., 2007).

More recently, forestry vehicles have been also increasingly considered for hybridization and introduction of hybrid electric powertrains (Fonseca et al., 2014; Potočnik and Poje, 2017; Karlušić et al., 2020) in order to provide significant gains in fuel economy, and also to facilitate measurable reductions in greenhouse gases emissions. This leads to many open questions in terms of forestry vehicles power distribution over such a complex hybrid power system, wherein components sizing and energy management control have great influence on the purchase cost and operating efficiency (Karlušić et al., 2020). The analysis by Karlušić et al. (2020) has pointed out to parallel hybrid power-train configuration as a good trade-off between fuel efficiency and

* Corresponding author.
E-mail addresses: matija.krznar@fsb.hr (M. Krznar), danijel.pavkovic@fsb.hr (D. Pavković), mihael.cipek@fsb.hr (M. Cipek).

https://doi.org/10.1016/j.egyr.2022.10.449

powertrain complexity, as also indicated by Cardoso et al. (2020). Parallel configuration is also beneficial from the point of view of conventional powertrain retrofitting with parallel-connected electrical drive (Karlušić et al., 2020). Due to the fact that heavy forestry machinery utilizes diesel engines as prime movers owing to their higher efficiency compared to gasoline-based engines, but also accounting for their less favorable pollutant emissions performance (Wang et al., 2022), forestry vehicle hybridization represents a paramount task, both from the fuel efficiency and emissions point of view (Karlušić et al., 2020).

These concerns have also arisen in other applications where diesel engine-based power production predominates, such as in isolated industrial facilities, as illustrated by Pavković et al. (2016b) and Kusakaka et al. (2021), renewable energy systems integration of diesel power-plants (Wang, 2020), and heavy railway freight haul (Cipek et al., 2019). However, when power flow and energy management control are concerned, coordinated control between different power sources needs to be precisely carried out in order to maintain prescribed voltage levels (Pavković et al., 2016a), while simultaneously achieving high fuel efficiency (Pavković et al., 2016b) with the electrical sub-system and power converters in particular operating at high overall efficiency values (Hassan et al., 2021).

Research efforts in control system design for coordinated control of multiple parallel DC/DC converters have encompassed a wide range of approaches. Montesinos-Miracle et al. (2013) have shown that conventional PI control can be rather effective in voltage balancing and current control of modular power converter designs with multiple DC/DC converters, which are frequently encountered in multi-level power converter applications, while Cimini et al. (2017) have shown that current sensor-less control scheme for voltage and current controlled DC/DC converter is achievable for the purpose of robust (current sensor fault tolerant) control based on nonlinear observer. Sarvi et al. (2014) have considered a PID controller optimized by means of particle-swarm optimization (PSO) and a fuzzy PID controller for controlling parallelized DC/DC converters, with fuzzy PID control offering distinct advantages in terms of closed-loop damping and input disturbance suppression. Beccuti et al. (2013) have considered a model predictive control (MPC) approach for synchronous control of multiple step-down (buck) converters, while also accounting for interleaved power converter operation, with the effectiveness of the proposed approach tested by means of simulations. Hamar and Toth (2009) have considered an agent-based decentralized control strategy for parallelized power converters and tested it experimentally. The main benefit of such parallel power converter array is in increased reliability and possibility of operation at optimal output efficiency by means of appropriate power converter scheduling. Distributed control of multiple parallel DC/DC converter based on consensus voting has been investigated by Moayedi and Davoudi (2014), and the resulting control system which augments the conventional proportional load sharing control strategy has been tested by means of simulations. Passivity-based control has been considered for individual power converters operating in parallel by Murakawa et al. (2020), and the resulting control system has been tested by means of simulations and experimentally. Even though advanced control strategies may improve the overall effectiveness of energy management and power flow control strategies, energy efficiency of the considered power converter topology represents another key aspect of power conversion system design (Li et al., 2019). To this end, Schön and Bakran (2015), Abdallah et al. (2011) and Li et al. (2019) have extensively investigated the DC/DC converter efficiency improvement measures with emphasis on DC/DC power converter topology choice and individual component design. However, the above research and development efforts in parallel power converter system design have been limited either to high-voltage stationary applications or low-scale (portable) systems, whereas applications in vehicular energy management systems have not been found in the available literature.

Having the above discussion in mind, the proposal of this paper is that a suitable parallel array of low-power DC/DC converters and an appropriate control strategy that coordinates power outputs of multiple parallelized DC/DC power converters using conventional proportional–integral (PI) control can facilitate effective energy management of the DC bus control system, and can also be extended so as to minimize the required number of active DC/DC power converters operating in parallel instead of a single high-power DC/DC converter. Such a power allocation system should have distinct advantages in terms of increased power conversion efficiency and reliability, while avoiding overheating issues and reducing the maintenance requirements. The main contribution of this paper is in the systematic analytical approach to primary-level and secondary-level control system design based on simplified linear process models and application of practical optima-based tuning of conventional proportional–integral controllers, which are typically encountered in practical applications. The proposed concept of tertiary-level control system using the input–output power efficiency of individual power converters within the parallel converter array represents the secondary contribution of this paper.

Hence, this paper investigates the effectiveness of one such parallelized low-cost DC/DC converter array suitable for the electrical power distribution system of a hybridized articulated forest tractor (also known as skidder). The resulting direct-current bus voltage and current control systems have been verified by means of detailed computer simulations and experimentally on the scaled-down laboratory setup of the DC bus of the electrified skidder power-train, with additional tests having been carried out related to power conversion efficiency mapping for the purpose of future tertiary-level control strategy development.

The paper is organized as follows. Section 2 describes the characteristics of the EcoTrac 120 V skidder and gives an overview of the power electronic components that are provided for the considered vehicle. Section 3 describes a solution for the integration of high-voltage and low-voltage energy system, and the development of computer models is explained. The control of the system is defined with an emphasis on the parallel operation of the converters is given in Section 4, while experimental verification is given in Section 5. Concluding remarks are given in Section 6.

2. Hybrid skidder and power electronics

The particular hybrid skidder is based on 7200 kg, EcoTrac 120 V vehicle, which is a heavy duty forestry tractor used for pulling logs out of the forest. It is manufactured by the Hittner company, located in the town of Bjelovar, Croatia (Hittner Tractors, 2021). Fig. 1a shows the main mechanical and electrical components of the conventional skidder power-train. The system consists of an ICE, friction clutches, ten-speed manual gearbox divided in five low-ratio road transport gears and five high-ratio working gears, mechanical shafts which transfer power to the forward (FD) and rear (RD) differentials which, in turn, distribute power to all four wheels (Knežević, 2010). The ICE considered herein is a four stroke diesel engine, manufactured by Deutz AG, type F6L-914. It is a naturally-aspirated 6.5 l six-cylinder in-line (straight-six), air-cooled, engine with maximum power rating P_e of 84 kW at 2300 min^{-1} and maximum engine torque T_e of 400 N m at 1500 min^{-1} (Deutz, 2004). The engine is started by an electrical engine starter powered by the onboard 24 V DC electrical system which is also used for powering electrical auxiliaries such

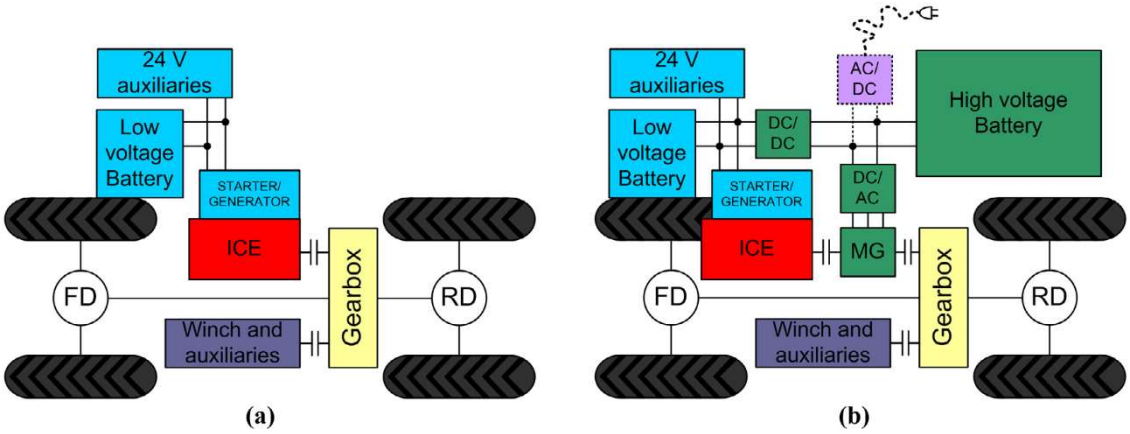

Fig. 1. Simplified representation of conventional skidder (a) and proposed hybrid vehicle configuration (b).

are lights, radio and similar. Skidders are also equipped with a double (or single) drum winch used for pulling logs, and a rear-side anchor-protective board, which also provides additional stability during winching operations. In a conventional skidder, the aforementioned winch system is driven by a hydraulic pump propelled by the mechanical power from the engine, which may also supply additional hydraulic actuators.

Off-road vehicles are increasingly being equipped with hybrid electric power-trains to improve their fuel economy, and, consequently, to facilitate notable reductions in greenhouse gases emissions. At the same time the size and power of the main diesel engine may be notably reduced through powertrain electrification using suitably sized electrical machines and battery energy storage, typically operating at relatively high direct-current (DC) voltages of about 450 V (Karlušić et al., 2020). Since most accessory loads still require the low-voltage (24 V DC) direct-current bus for their power supply, two direct-current electrical systems are commonly present within such hybrid vehicles (Fig. 1), whereas the low-voltage DC bus may be supplied by the high-voltage battery by using step-down (DC/DC) power converters.

The principal requirement of hybridization is maintaining the performance of the hybrid drive at least equal to the conventional one, while simultaneously minimal modifications to the overall power-train are preferable from the production point of view. In that respect, the maximum loading capabilities of the particular forestry vehicle should also be respected. A P2 parallel hybrid configuration (shown in Fig. 1b) is proposed herein, which satisfies the predefined driving performance, and also does not require major modifications of the conventional power-train for its installation (Karlušić et al., 2020). Thus, the chosen P2 parallel configuration may also be convenient from the standpoint of conventional power-train retrofitting to its hybrid counterpart. As Fig. 1b shows, the hybrid skidder has an additional electric motor (MG), a clutch and a properly sized additional high-voltage (450 V DC) battery according to Karlušić et al. (2020) in order to store sufficient amounts of electric energy for the anticipated operating cycle of the vehicle.

The electrical part of the hybrid skidder contains additional power electronics components (see Fig. 1b). As with a conventional skidder, the auxiliary components are powered by an auxiliary 24 V battery. A DC/DC converter is connected between the auxiliary battery and the main battery, and it is used to step-down the voltage of the main battery to the voltage of the auxiliary battery. If it is a rechargeable hybrid vehicle then there is also an additional AC/DC charger that can recharge the battery from the mains voltage (Mi et al., 2017). A DC/AC power converter (inverter) is used to control the power flow between the battery and the electric motor. During regenerative braking, when the motor works as a generator producing AC current and voltage, these quantities are rectified to their respective DC counterpart by the inverter operating in the active rectifying regime, thus charging the battery. On the other hand, when the electric motor propels the vehicle, the DC current from the battery is converted into AC current by means of the aforesaid inverter thus supplying the electric motor. Note that the efficiency of power conversion within the aforementioned power electronics devices has a significant impact on the overall energy efficiency of the vehicle.

Although there are similarities between energy converters used in hybrid vehicles and those used in industrial and other applications, there are certain particular features specific to their application in motor vehicles. One example is the need for wider operating temperature range, insensitivity to mechanical vibrations, special requirements regarding electromagnetic compatibility and thermal control (Mi et al., 2017). Power converters are usually classified according to their input and output voltage and current shapes, thus resulting in four main categories: DC/DC converters, DC/AC converters or inverters, AC/DC converters or rectifiers and AC/AC converters. In hybrid vehicle applications DC/DC converters are used for voltage/current level shifting (step up or step down), whereas inverters are either used for DC to AC voltage/current conversion during motoring operation or AC/DC conversion (active rectifying) during regenerative braking (Mi et al., 2017). Finally, embedded active rectifiers, either as discrete components or as a part of main electric motor inverter (Yilmaz and Krein, 2013) are used for battery charging from the utility grid. Depending on voltage levels, either MOSFETs or IGBTs are used as power switching devices, with power Schottky diodes typically being used for switching transient suppression (snubbing), with switching frequencies typically not exceeding 10 kHz. Power electronic converters (especially those for mains grid applications) are typically equipped with an LC or LCL filter for the suppression of high-frequency (switching) harmonics in the inverter/active rectifier grid-side voltage and current (Zhong and Hornik, 2013).

3. Integration of high-voltage and low-voltage DC system

This section presents the integration of high-voltage (450 V DC) and low-voltage (24 V DC) system by means of step-down DC/DC converters, and the derivation of a suitable control and simulation oriented dynamic model of power converter.

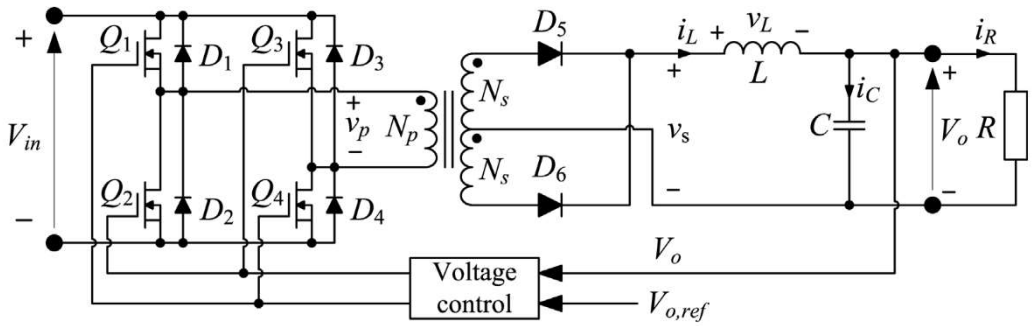

Fig. 2. Topology of isolated "buck" (step-down) DC/DC converter (Liu, 2017).

3.1. DC/DC converter

In order to integrate high voltage DC link from the main battery to a lower voltage DC bus (i.e. from 450 V to 24 V) and to charge the auxiliary battery a dedicated DC/DC converter is needed. For safety reasons, the lower voltage system must be insulated from the high voltage side, so the DC/DC converter must be an insulated "buck" (or step-down) converter. The topology of such insulated "buck" (step-down) converter is shown in Fig. 2.

This inverter has two switching modes and four operating modes. During the first subinterval of the first overlap period, MOSFET switches Q_1 and Q_4 are ON while switches Q_2 and Q_3 are OFF, while during the second subinterval, all switches are off. During the first subinterval of the second switching period, MOSFET switches Q_1 and Q_4 are OFF while switches Q_2 and Q_3 are ON, and during the second subinterval of this interval all switches are off. In this way, a bipolar AC voltage is generated at the transformer primary winding, which is rectangular in shape (Liu, 2017). During the first subinterval of the first switching period in which the Q_1 and Q_4 switches are on and Q_3 and Q_2 are off on time t_{on}, the voltage of the primary winding of the transformer is equal to $v_p = V_{in}$ and the diode D_5 conducts. During this period of time, the voltage of the secondary winding of the transformer amounts to (Liu, 2017):

$$v_s = kv_p = \frac{N_s}{N_p} v_p, \tag{1}$$

where N_s is the number of secondary windings, N_p is the number of primary windings, and v_p is the voltage of the primary winding of the transformer. The voltage v_L of the inductor coil (choke) is then obtained according to the following expression (Liu, 2017):

$$v_L = v_s - V_o = \frac{N_s}{N_p} v_p - V_o = \frac{N_s}{N_p} V_{in} - V_o, \tag{2}$$

where V_{in} is the input voltage, v_s the secondary voltage, v_p the primary voltage and V_o the resistor voltage (output voltage).

During the second subinterval of the first switching period in which all switches (Q_1, Q_2, Q_3 and Q_4) are switched OFF at t_{off} time, the voltage of the primary winding of the transformer is equal to zero and both diodes D_5 and D_6 are conducting. During this time period, the voltage of the inductor coil L is equal to the output voltage $v_L = V_o$. The current flowing through the inductor i_L can be represented as (Liu, 2017):

$$v_L(t) = L\frac{di_L(t)}{dt} \Rightarrow i_L(t) = \begin{cases} \frac{1}{L}\int_0^t \left(\frac{N_s}{N_p} V_{in} - V_o\right) dt = i_L(0) \\ \quad + \frac{1}{L}\left(\frac{N_s}{N_p} V_{in} - V_o\right) t, \quad 0 \le t \le t_{on} \\ \frac{1}{L}\int_{t_{on}}^t V_o dt = t_L(t_{on}) - \frac{V_0}{L} t, \quad t_{on} \le t \le T_s \end{cases}, \tag{3}$$

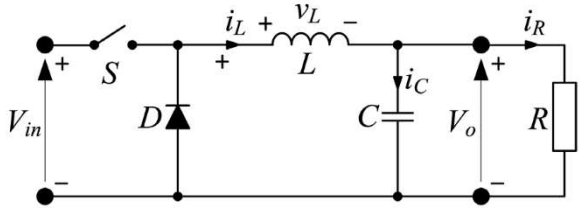

Fig. 3. Simplified topology of "buck" DC/DC converter (Luo and Ye, 2016).

where is L the inductance of the coil, t_{on} is switching on time and T_s is the half switching time.

During the first interval of the second switching interval, switches Q_1 and Q_4 are OFF and switches Q_2 and Q_3 are turned ON at the same time, thus resulting in the primary winding voltage being opposite in sign to the input DC bus voltage V_{in}. Hence, diode D_6 conducts at the secondary of the transformer. The principle of operation of the output filter (inductor) and the load voltage drop is the same as in the case of first subinterval (Liu, 2017). If Kirchhoff's voltage law is applied to the inductor, the following relationship between the output and input voltages of the DC/DC converter are obtained (Liu, 2017):

$$V_o = \frac{N_s}{N_p} V_{in} \frac{t_{on}}{T_s} = \frac{N_s}{N_p} V_{in} d, \tag{4}$$

where d is the switching waveform duty cycle. The output voltage is then controlled by varying (modulating) the width of the switch-chopped input pulse (the so-called pulse-width modulation or PWM), which determines the duration of the time each electronic switch is either open or closed within a single switching cycle (Keng, 2016).

3.2. Simplified computer simulation model of DC/DC converter

The basic topology of a step-down or buck DC/DC converter is shown in Fig. 3. This simplified model has similar behavior, and is used to create a simplified switching-based computer simulation model (Keng, 2016).

The operation of the converter can be described by two differential equations, one describing the inductor current dynamics, and the other describing the output voltage dynamics. For each switch S state (ON; $S = 1$ or OFF; $S = 0$) the equations are then:

$$\frac{di_L}{dt} L = SV_{in} - V_o, \tag{5}$$

$$\frac{dV_o}{dt} C = i_L - \frac{V_o}{R}. \tag{6}$$

Because this model incorporates highly-nonlinear voltage switching phenomena, it is numerically inefficient. Hence, for simulation

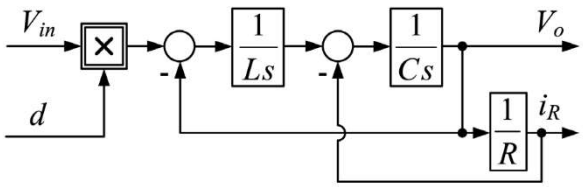

Fig. 4. Averaged model of "buck" DC/DC converter.

studies it is more convenient to use an averaged model shown in Fig. 4. This model calculates the converter output voltage based on input voltage and the PWM duty cycle factor.

4. Control system design

This section presents the primary secondary and tertiary level control of the common DC bus based on embedded voltage and current controllers within individual DC/DC power converters, and the superimposed load sharing control strategy, respectively. The design of individual controllers is based on the damping optimum criterion (Naslin, 1968).

4.1. DC power distribution systems hierarchical control overview

Hierarchical control architecture is used in many power distribution systems, such as those within DC microgrids (Gao et al., 2019). The hierarchical control system arrangement comprises of the primary, secondary and tertiary control levels (control layers), as shown in Fig. 5, wherein the primary control level deals with current/voltage control, the secondary control level deals with voltage sag compensation, load sharing and power quality improvement measures, and the highest-level control (tertiary control layer) deals with power and energy management and energy system performance optimization. Such hierarchical control system arrangement is facilitated by simultaneously using communication link-based coordinated control (Gao et al., 2019).

PI controller design suitable for embedded voltage and current control is proposed for the primary-level control within the DC–DC power converter module. For the secondary control level, a centralized load sharing control strategy based on PI controller of the common DC bus voltage is presented.

4.2. Damping optimum criterion

The control system design herein is carried out according to the damping optimum criterion (Naslin, 1968). This is a pole-placement-like analytical method of design of linear continuous-time closed-loop systems, with the tuning procedure based on the following closed-loop characteristic polynomial:

$$A(s) = D_2^{n-1} D_3^{n-2} \cdots D_n T_e^n s^n + \cdots + D_2 T_e^2 s^2 + T_e s + 1, \tag{7}$$

where T_e is the closed-loop system equivalent time constant, and $D_2, D_3, \ldots, D_n$ are the so-called characteristic ratios.

In the optimal case $D_i = 0.5$ $(i = 2 \ldots n)$, the closed-loop system of any order n has a quasi-aperiodic step response characterized by an overshoot of approximately 6% (resembling a second-order system with damping ratio $\zeta = 0.707$) and the approximate rise time $(1.8 - 2.1)\cdot T_e$. For larger T_e value choices, the dominant closed-loop modes are characterized by slower response and generally improved control system robustness and noise suppression ability.

From the standpoint of designing of a superimposed controller, the inner closed-loop system tuned according to the damping optimum criterion may be approximated by the equivalent first-order lag transfer function characterized by the closed-loop equivalent time constant T_e (under assumption of unit gain of the inner closed-loop system):

$$G_e(s) = \frac{1}{T_e s + 1}, \tag{8}$$

4.3. Primary-level voltage/current control

Block diagram of the DC/DC buck converter output voltage control system featuring proportional–integral (PI) voltage and current feedback controllers in the so-called cascade control system arrangement (Schröder, 2007) is shown in Fig. 6, wherein the voltage PI controller commands the current reference to the inner current control loop. This facilitates straightforward limiting of the buck converter current i_c via the current limit I_{max} (Pavković et al., 2014). The buck converter voltage reference u_R is supplied from the secondary control level (see next subsection), wherein the voltage target is low-pass filtered in order to avoid unnecessary voltage reference step overshoots due to the PI controller zero $(s_z = -1/T_{cu})$.

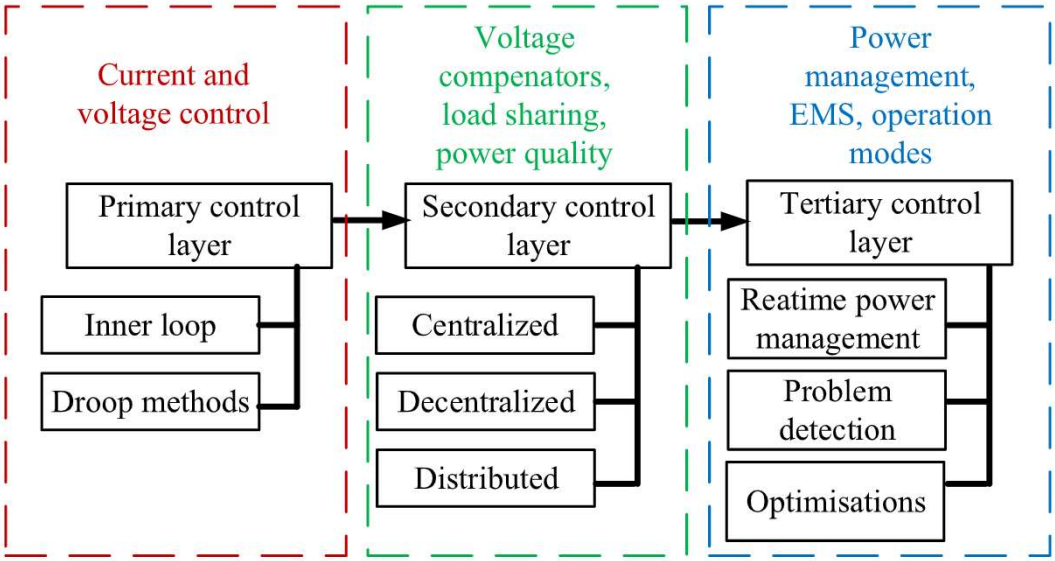

Fig. 5. Hierarchical control system overview (Gao et al., 2019).

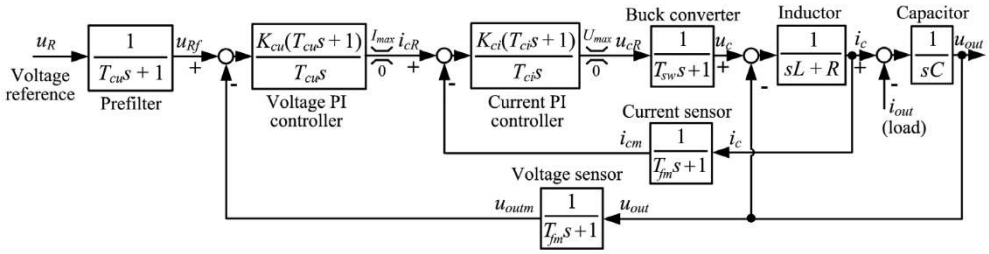

Fig. 6. Buck converter cascade control system structure with voltage/current PI controllers.

For the purpose of current control loop design, the fast lag terms corresponding to PWM switching delay T_{sw} and current sensor delay T_{fm} are lumped into a single lag term with equivalent "parasitic" time constant $T_{\Sigma i} = T_{sw} + T_{fm}$, which may also comprise the controller sampling time parameter if digital controller is considered. In addition, the quite slow output capacitor charging/discharging dynamics (output voltage u_{out} dynamics) may typically be neglected in current controller design. Applying the zero-pole canceling approach to cancel out the largest open-loop time constant (i.e. inductor time constant L/R herein) by the PI controller zero (Schröder, 2007), results in the following integral time constant T_{ci} choice:

$$T_{ci} = \frac{L}{R}, \tag{9}$$

which, in turn, yields the following current control loop transfer function model:

$$G_{ci}(s) = \frac{i_{cm}(s)}{i_{cR}(s)} = \frac{1}{\frac{T_{ci}T_{\Sigma i}}{K_{ci}}s^2 + \frac{RT_{ci}}{K_{ci}}s + 1}, \tag{10}$$

By equating the coefficients of the current control loop characteristic polynomial in (10) with the characteristic polynomial (7) according to damping optimum criterion, the following final expressions for current PI controller parameters are obtained:

$$T_{ei} = \frac{T_{\Sigma i}}{D_{2i}}, \quad K_{ci} = R\frac{T_{ci}}{T_{ei}}. \tag{11}$$

Similarly, in the case of voltage feedback control system design, the equivalent lags of the current control loop T_{ei} and the voltage sensor T_{fm} are lumped into an equivalent lag term with time constant $T_{\Sigma u} = T_{ei} + T_{fm}$, (with the possibility of including the controller sampling time, if needed). By applying the damping optimum criterion to the voltage feedback loop characterized by the above approximation of the fast-inner loop dynamics, the following expressions for parameters of the voltage PI controller are obtained (Pavković et al., 2016a):

$$T_{cu} = T_{cu} = \frac{T_{\Sigma u}}{D_{2u}D_{3u}}, K_{cu} = \frac{C}{D_{2u}T_{eu}}. \tag{12}$$

4.4. Secondary-level load sharing control

Fig. 7 shows the schematic of the load sharing topology where high-voltage DC power supply parallel-connected DC/DC buck converter. In this arrangement, the parallel-connected and output voltage-controlled buck converters are connected to the common low-voltage DC bus (characterized by its "smoothing" capacitor capacitance C_{dc}) through series blocking diodes $D_{b1} \ldots D_{b,n}$, which prevent reverse current flow (current can flow from into the DC bus). A battery energy storage system (BESS), characterized by its electromotive force E_b and internal resistance R_b, is also connected in parallel to the DC bus.

Under normal operating conditions, voltage-controlled buck converters can supply the DC bus up to their internal current

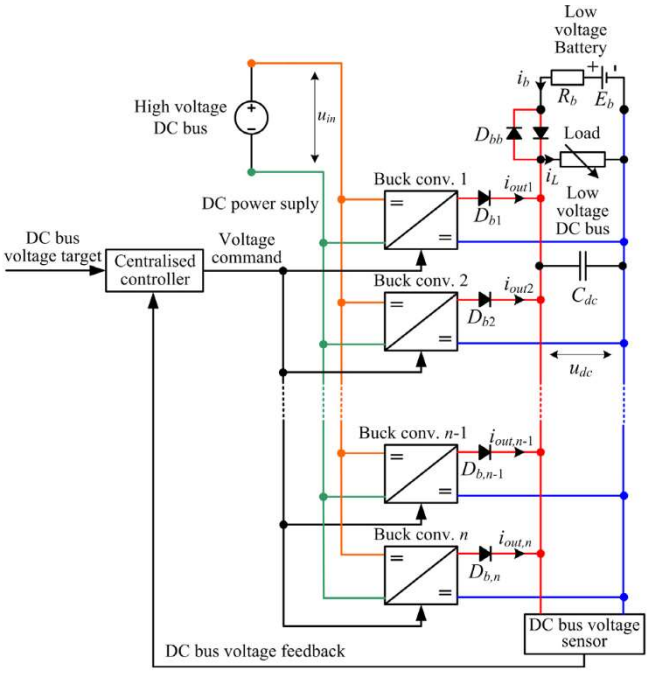

Fig. 7. Schematic representation of load sharing topology with centralized controller.

limits I_{max} (see Fig. 6). When the DC bus load exceeds the collective maximum current $\max(\Sigma i_{out}) = \max(i_{out1} + i_{out2} + \cdots + i_{out,n-1} + i_{out,n}) = nI_{max}$ (where n is the number of parallel-connected buck converters), the DC bus voltage should exhibit a noticeable droop (sag) behavior. Difference between the battery electromotive force E_b and the DC bus voltage u_{dc} determined a battery charging or discharging where current is determined by the battery internal resistance R_b (i.e. $i_b = (E_b - u_{dc})/R_b$). Fig. 8 shows the block diagram representation of the load sharing control strategy based on the topology in Fig. 7, wherein a proportional–integral PI controller is used for DC bus voltage control based on DC bus voltage sensor feedback.

Again, the centralized PI feedback controller is designed according to the damping optimum criterion. For that purpose, the parallel-connected bank of voltage-controlled buck converters is assumed to have equal static and dynamic properties, i.e. to be characterized with equal voltage reference lags T_{eu}, as well as the blocking diode forward polarization voltage u_F and dynamic resistance r_d during diode conduction (forward biasing). In that case, the parallel-connected DC/DC power converter stack can be represented by the following equivalent model under forward biasing assumption for all blocking diodes:

$$G_p(s) = \frac{\Sigma i_{out}(s)}{u_{Rp}(s)} = \frac{1}{\frac{r_d C_{dc}}{n}s + 1} \cdot \frac{1}{T_{eu}s + 1} \tag{13}$$

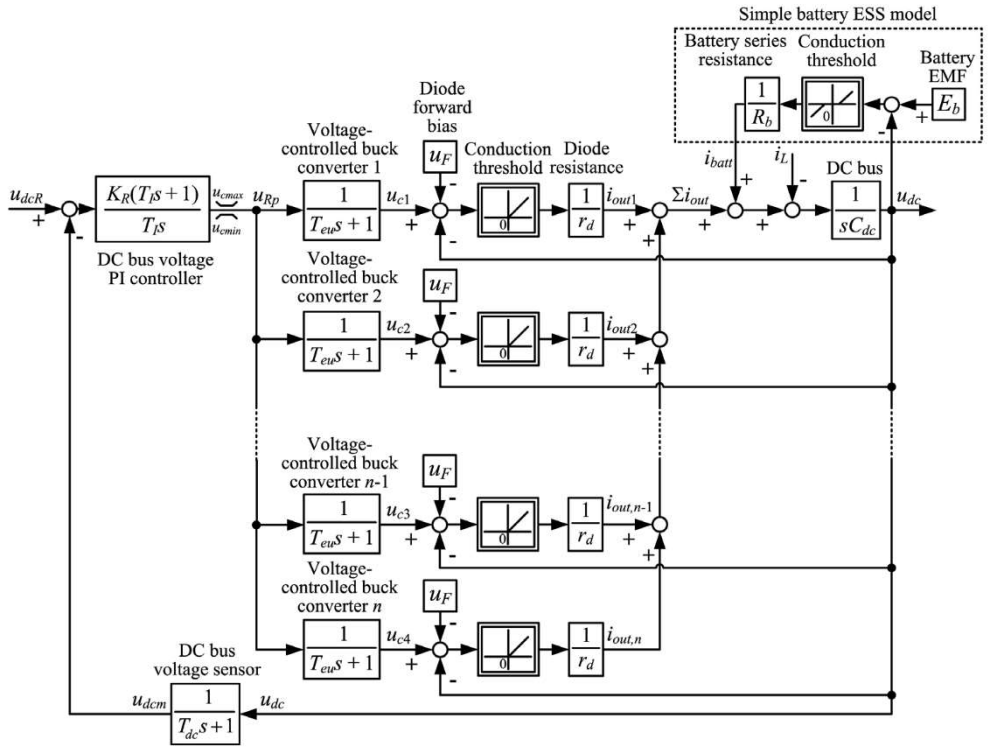

Fig. 8. Block diagram of centralized load sharing strategy for DC bus voltage control.

By lumping the DC bus voltage sensor time constant T_{dc} with the DC bus charging time constant $C_{dc}r_d/n$, the resulting lag term with time constant $T_{\Sigma dc} = T_{dc} + C_{dc}r_d/n$ (which may also include controller sampling effects in the case of digital controller) is used as a basis for PI controller damping optimum design. In the above case, the closed-loop transfer function characteristic polynomial reads as follows:

$$A_{cl}(s) = \frac{T_{eu}T_{\Sigma dc}T_I}{K_R}s^3 + \frac{(T_{eu}+T_{\Sigma dc})T_I}{K_R}s^2 + \frac{1+K_R}{K_R}T_I s + 1. \quad (14)$$

By equating the above characteristic polynomial with the damping optimum characteristic polynomial (7), the following expressions for centralized PI controller parameters (closed-loop equivalent time constant T_{edc}, and controller proportional gain and integral time constant K_R and T_I) are obtained after some manipulation and rearranging:

$$T_{edc} = \frac{1}{D_{2dc}D_{3dc}}\frac{T_{eu}T_{\Sigma dc}}{T_{eu}+T_{\Sigma dc}},$$

$$K_R = \frac{T_{eu}+T_{\Sigma dc}}{D_{2dc}T_{edc}} - 1, \quad (15)$$

$$T_I = T_{edc}\left(1 - \frac{D_{2dc}T_{edc}}{T_{eu}+T_{\Sigma dc}}\right)$$

4.5. Tertiary-level power management control

One possible solution implementing the tertiary level control is to switch ON and OFF the parallel-connected DC/DC converters depending on the load conditions at the low-voltage DC bus. By measuring the output power, the operating conditions for each DC/DC converter is determined, and the efficiency of each individual converter can be estimated by using the pre-recorded power conversion efficiency maps. Maximum output power of each converter determines the minimum number of required operating converters to supply the requested load. The total system efficiency η_{tot} with n converters is then calculated according to the following expression:

$$\eta_{tot} = \frac{\sum_{i=1}^{n} P_{o,i}}{\sum_{i=1}^{n} \frac{P_{o,i}}{\eta_i}}, \quad (16)$$

where η_i and $P_{o,i}$ are the efficiency and the output power of the ith converter. The program logic then maximizes η_{tot} and turns ON/OFF individual converters. Furthermore, it is possible to implement an optimization algorithm such as that would maintain the highest efficiency of the system depending on the load, measure the operating time of individual inverters and equalize the amount of operating time to reduce the heat load and maintenance requirements.

5. Simulation and experimental results

The proposed DC/DC buck converter voltage/current control system and the centralized controller-based load sharing strategy are verified by means of simulations within MATLAB/Simulink™ software environment. The load sharing strategy is also verified experimentally on the dedicated laboratory setup featuring off-the-shelf DC/DC step-down (buck) converters (Droking.com, 2021), whose parameters are listed in Table 1.

5.1. Results of simulation verification of primary and secondary control levels

The parameters of control-oriented process models and controllers used in the simulation study are listed in Table 2, wherein models of the buck converter and lithium-polymer battery have been parameterized based on data from Droking.com (2021), Genspow GmbH (2021), ON Semiconductor (2017), Infineon Technologies AG (2006) and McPower (2021).

Fig. 9 shows the buck converter cascade control system responses for the case of load step change from zero to 20 A. The buck converter output voltage u_{out} is characterized by a 0.9 V

Table 1
DC–DC buck converter specifications from supplier (Droking.com, 2021).

Converter type	Description
Model	AP-D5830A
Input voltage	20–70 VDC
Input current	Max. 20 A
Output voltage	2.5–58 V
Output current limit	0.1–30 A
Output power	Max. 800 W
Idle current	<70 mA (24 V in/12 V out)
Output voltage ripple	<120 mV (24 V in/12 V out)
Rated efficiency	0.93–0.97
Switching frequency	150 kHz
Dimensions	154 mm × 75 mm × 70 mm
Mass	0.6 kg

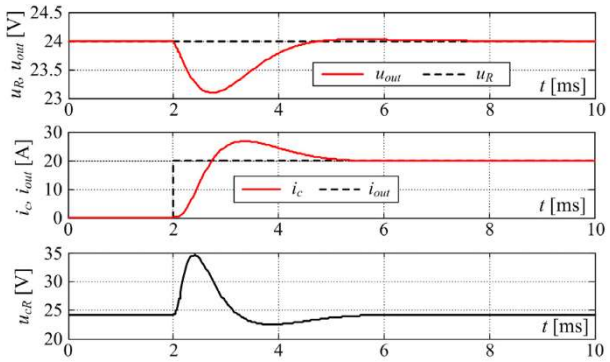

Fig. 9. Simulation results of buck converter output voltage cascade control system.

drop (3.75% drop from the target value $u_R = 24$ V), with output voltage recovery within 2.5 ms (top plot in Fig. 9). Such favorable load suppression ability is obtained due to fast response of inner current control loop under voltage/current cascade control arrangement (middle and lower plot in Fig. 9).

Fig. 10 shows the simulation results of the centralized controller-based load sharing control strategy for two characteristic operating regimes: (i) the so-called small-signal regime (Fig. 10) characterized by a relatively small load change and operation of all buck converters well within voltage/current limit values, and (ii) the large signal regime (Fig. 10) characterized by large load change and buck converter operation at voltage/current limit values. In the case of small signal operation, the centralized load sharing control system is characterized by a relatively small transient DC bus voltage drop after the DC bus load current change, particularly for a 20 A load current step, a 0.75 V DC bus voltage drop is observed (i.e. only 3.1% of the DC bus voltage target value of 24 V), characterized by 15 ms recovery time and settling within 50 ms of the load step instant (top plot in Fig. 10). This control system performance is achieved primarily by means of DC/DC buck converter action, whose joint current supply to the DC bus Σi_{out}, commanded by the centralized PI controller via buck converter voltage reference change (bottom plot in Fig. 10) predominantly compensates for the transient DC bus voltage drop and stead-state load i_L in order to maintain the DC bus equilibrium state (middle plot in Fig. 10). The battery also compensates the DC bus load (albeit briefly) when the DC voltage drops. On the other hand, when the load sharing strategy operates in the large signal regime (characterized by 120 A load current step change), the DC bus voltage is characterized by a relatively small steady-state error of 1.1 V (4.6% of the DC bus voltage target value), as shown in the top plot in Fig. 10b. The battery is supplying the current excess with respect to the joint current limit of four buck converters connected in parallel ($n_{conv} I_{max} = 100$ A, see Table 2), as illustrated by the middle plot in Fig. 10b. Due to current limiting action of individual buck converters, the voltage command supplied by the superimposed PI controller cannot provide for the additional control authority, and is effectively limited to the maximum value of the buck converter output voltage (bottom plot in Fig. 10b). These results are going to be used as a benchmark for the experimental examination of the parallelized power converter operation under the proposed control scheme.

5.2. Experimental verification of load sharing centralized control strategy

The experimental setup (shown in Fig. 11) consists of the stand, DC power supply, two DC–DC buck converters, lithium-polymer (LiPo) battery, DC link (DC bus) and related capacitors, diodes, current and voltage sensors and a microcomputer control unit (Arduino Mega) that enables PC-based data acquisition and control. Technical specifications of individual control system components are given in Table 3.

Table 2
Parameters of primary and secondary level control simulation models.

Symbol	Description	Value
C_{out}	Buck converter output capacitor capacitance	10 mF
L	Buck converter inductor inductance	0.3 mH
R	Buck converter inductor internal resistance	5 mΩ
T_{sw}	Buck converter PWM switching delay ($T_{sw} = 1/f_{sw}$)	0.05 ms
T_{fm}	Buck converter voltage/current sensor time constant	0.5 ms
u_F	Blocking diode forward biasing voltage	0.7 V
r_d	Blocking diode conduction resistance	20 mΩ
E_b	Lithium-polymer battery electromotive force	24 V
R_b	Lithium-polymer battery series resistance	20 mΩ
I_{max}	Buck converter output current limit	25 A
U_{max}	Buck converter output voltage limit	36 V
K_{ci}	Primary level current PI controller proportional gain	0.19 A/A
T_{ci}	Primary level current PI controller integral time constant	60 ms
K_{cu}	Primary level voltage PI controller proportional gain	2.13 V/V
T_{cu}	Primary level voltage PI controller integral time constant	9.4 ms
C_{dc}	DC bus capacitor capacitance	100 mF
T_{dc}	DC bus voltage sensor filtering time constant	1.5 ms
u_{cmax}	Centralized controller output upper voltage limit	36 V
u_{cmin}	Centralized controller output lower voltage limit	20 V
n_{conv}	Number of parallel-connected buck converters	4
K_R	Centralized load sharing control PI controller proportional gain	2.21 V/V
T_I	Centralized load sharing control PI controller integral time constant	7.1 ms

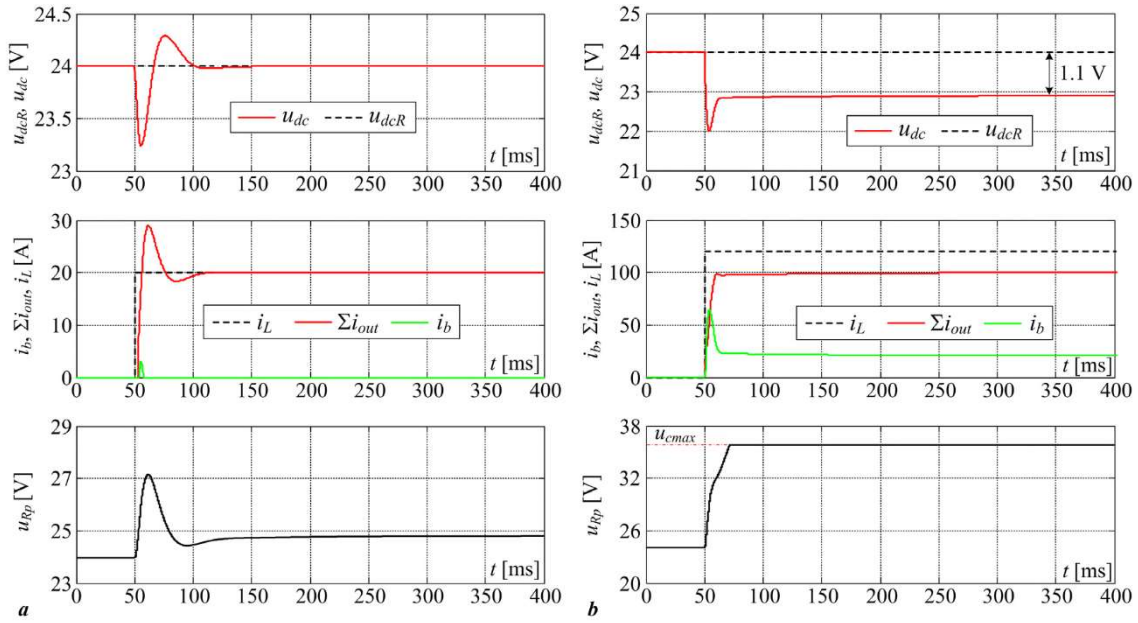

Fig. 10. Simulation results of centralized secondary-level load sharing control strategy: small-signal regime (a) and large signal regime (b).

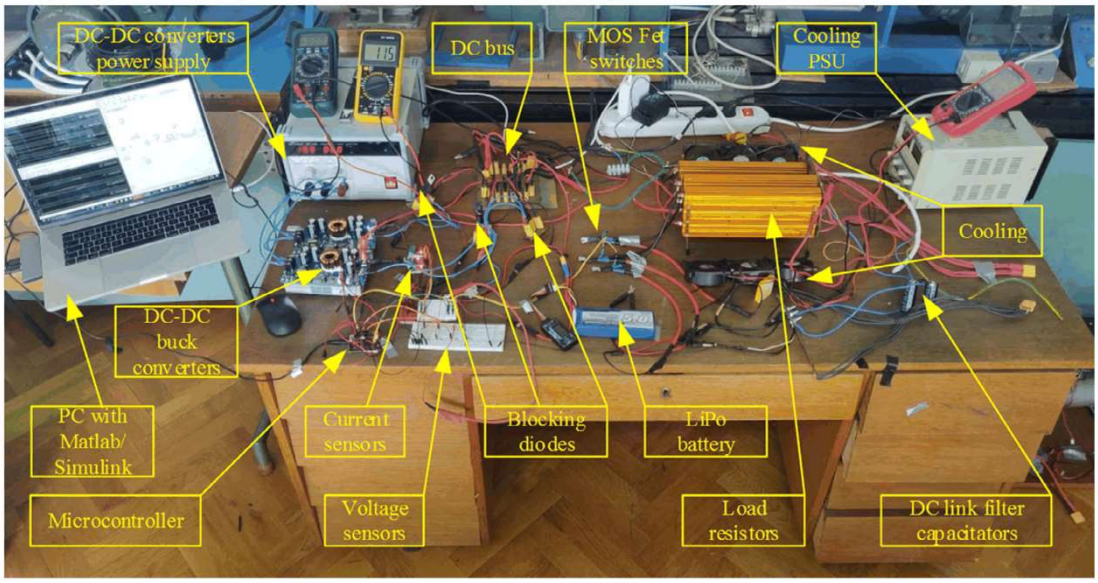

Fig. 11. Photograph of the laboratory experimental setup.

Fig. 12 shows the experimental results of the centralized controller-based load sharing strategy for three characteristic operating regimes: low power (2.2 Ω, one load resistor active), 1.1 Ω (two load resistors active in parallel) and 0.73 Ω (three load resistors active in parallel). For safety reasons, the load sharing control system has been tested at reduced power and voltage (i.e. a three cells in series lithium-polymer battery with terminal voltage of 12 V, and 10 A of maximum total load current). Also note that the experimental scenario differs from the simulation benchmark in terms of number of available power converters, but the principle of operation is easily generalized to an arbitrary number of power converters operating on the experimental test-bed. In the case small and medium load, current is primarily supplied by the two buck converters used in this case. Load sharing depends on voltage references fed to DC converters and shows good performance. In the case of large load DC–DC converters are outputting their maximum currents (about 4 A each), and the remaining current drain is obtained from the battery after the DC bus voltage drops below the level required for forward biasing of the current blocking diode connected in series with the battery. These results generally confirm the results obtained by the simulation benchmark and are a good indication that the proposed centralized control approach can be used with an arbitrary number of parallelized DC/DC buck power converters. The presence of relatively high-frequency noise in the DC/DC converter current i_2 (and to some extent in currents i_L and i_1) should also be noted. It is likely caused by irregular external noise (outliers in DC bus voltage measurement due to external electromagnetic interference) that the low-pass filter on-board the experimental set-up was not able to completely suppress. This sporadic noise subsequently resulted in perturbed voltage references to individual DC/DC power converters, which is amplified in the output current signal due to the implicit derivative action of the inner current control loop within the power converter with

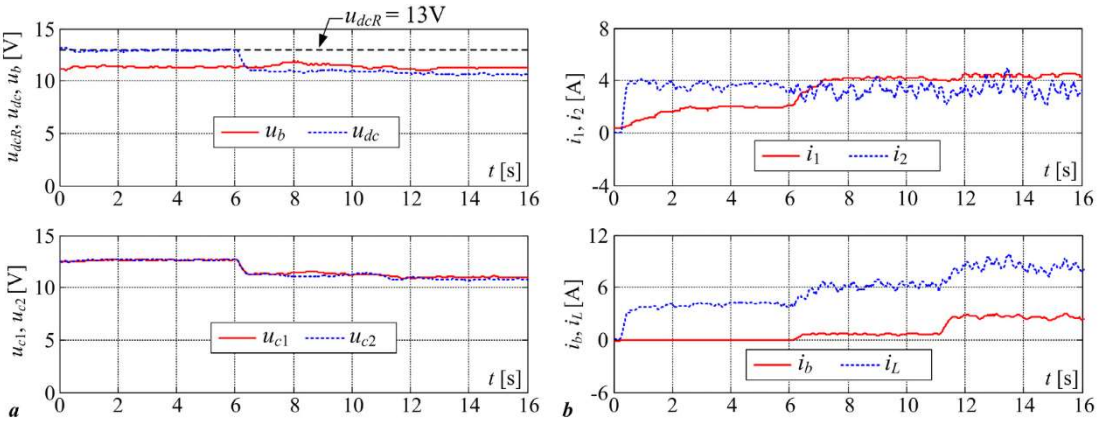

Fig. 12. Experimental results of centralized load sharing control strategy.

Table 3
Technical specifications of control system components used in experimental setup.

Component	Description
Buck DC–DC	800 W, non-isolated topology, 20–70 V input, 2.5–58 V output, maximum input current 20 A, maximum output current 30 A
DC–DC converters power supply	Laboratory grade high power DC switching power supply with current limiting and voltage regulation. 0–30 V, 0–50 A
DC bus	Common positive and negative terminal for connection of loads and sources, implemented with XT60 connectors
Current sensor	ACS712 hall effect sensor, 20 A
Voltage sensor	Voltage divider with transfer ratio 11.0
Diode	High voltage Schottky rectifier diode, $u_F = 0.37$ V, $I_{max} = 250$ A
Load switches	Logic level n-channel MOSFET, IRLZ44, $V_{dss} = 60$ V, $I_d = 27$ A
Filter Capacitors	1200 μF, electrolytic, 63 V
Battery	Lithium-polymer (LiPo) 5000 mAh, 5 C
Load resistors	2R2 (2.2 Ω)/500 W
Computer	MBP 2018 with Matlab/Simulink
Microcontroller	Arduino Mega
Cooling PSU	Laboratory grade switching power supply with current limiting and voltage regulation. 0–30 V, 0–3 A
Cooling fans	60 mm cross section PC cooling fan, 12 V power supply

respect to voltage reference (see analysis related to Fig. 6):

$$\frac{i_c(s)}{u_R(s)} \approx \frac{C}{K_{cu}} \cdot \frac{s}{\frac{T_{cu}T_{\Sigma uC}}{K_{cu}}s^3 + \frac{T_{cu}C}{K_{cu}}s^2 + T_{cu}s + 1}. \tag{17}$$

Due to the aforementioned power converters being off-the shelf components, their voltage input–output bandwidths and reference noise suppression characteristics may slightly differ, which may in turn produce different levels of the noise in the power converter voltage reference path.

5.3. Experimental identification of efficiency curves

The converter efficiency measurement can be carried out by connecting the DC/DC converter to a variable DC voltage source, and variable load provided by a dissipating resistors network. Fig. 13a shows the schematic representation of the experimental setup, along with the actual photo (Fig. 13b). For different loads, i.e. different combinations of 2 Ω resistors, the efficiency will be measured for resistance values of 4.04 Ω, 3.05 Ω, 2.04 Ω, 1.67 Ω, 1.34 Ω and 1.01 Ω. The input voltage for each load is varied from 40 V to 60 V in increments of 5 V. The output voltage is maintained constant of 24 V. The converter efficiency η_{cm} can be than calculated as the ratio of input P_{in} and output P_o power, as follows:

$$\eta_{cm} = \frac{P_o}{P_{in}} = \frac{\frac{V_o^2}{R}}{V_{in}I_{in}}. \tag{18}$$

Fig. 14a shows the results of efficiency estimation with respect to the power converter input voltage and output power. Average efficiency value η_{cma} over the range of considered voltages is shown in Fig. 14b. The obtained results show that the efficiency increases with the increase of the output power until the load reaches approximately 35% of the maximum converter power output, at which point it gradually decreases with the further load increase. Fig. 14a also shows that the DC power converter efficiency also depends on the input voltage, and is highest at 50 V for the particular converter. These results also show that if the converter operates at boundary load values (i.e. either at low or high load) the efficiency would generally be lower, which means that converters obviously have a point of operation with highest efficiency (Fig. 14b). These results could be useful for power management control system design in which the number of engaged parallel converters is determined based on the requirement that the power load of each converter currently in operation should be close to 35% of the rated power output.

6. Conclusion

The paper has investigated primary and secondary level control of a parallelized low-cost DC/DC converter array intended to be used for the hybrid vehicle integration of high-voltage energy system and low-voltage energy system. The primary-level control of individual DC/DC power converters has been based on the cascade control system arrangement and voltage and current PI controllers. Similarly, PI voltage controller has been used for the secondary-level centralized control of the DC bus voltage via parallel operation of DC/DC power converters, with the auxiliary battery handling the excess DC bus load. The control system design has been based on the damping optimum criterion.

The proposed control systems have been verified by means of comprehensive computer simulations and experimentally on the test setup. Results have shown that the primary-level cascade control of the DC/DC power converter can provide fast and well-damped closed-loop responses, with the voltage drop after the step load change of 80% rated value resulting in only 3.75% output voltage drop and recovery time of about 3 ms. Similar voltage control system behavior has been observed for the case

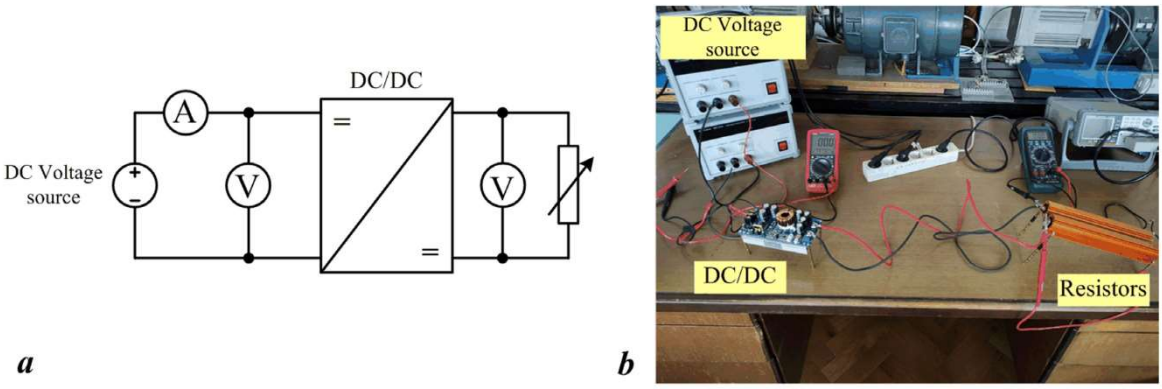

Fig. 13. Schematic representation (a) and photograph (b) of laboratory experimental setup for efficiency measurement.

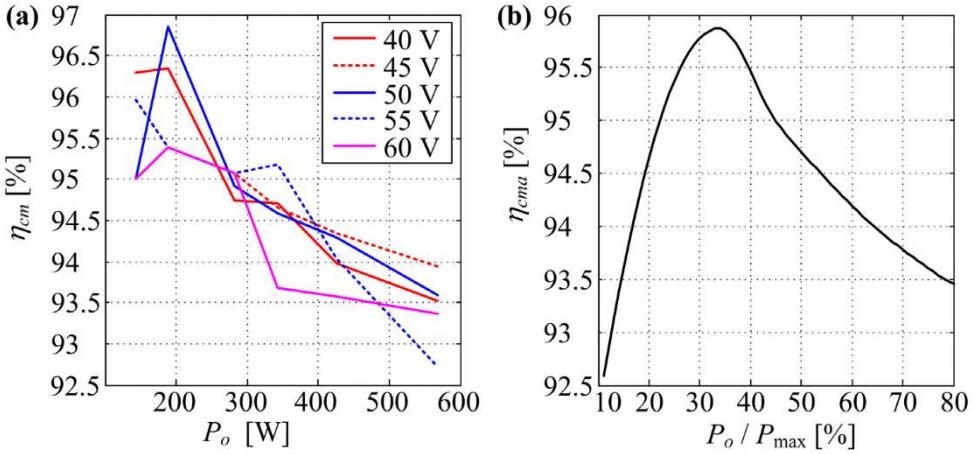

Fig. 14. Efficiency measurements (a) and average efficiency characteristic (b) of DC/DC step-down converter under investigation.

of secondary-level control using a parallel array of DC/DC converters, with slower voltage recovery response (15 ms voltage restoration lag) due to inherent lag of the DC bus control loop. When the collective current limit of parallelized DC/DC power converters is exceeded, the auxiliary battery effectively covers for the excess load, and the overall control system dynamics remain well-damped.

The experimental setup has also been used to parameterize the power losses of the individual DC/DC converter and map its power conversion efficiency. The results have shown that the particular step-down DC/DC converter array has the optimum efficiency operating point at approximately 35% of the rated power output. This indicates that the prospective tertiary-level control strategy should implement load sharing between parallelized power converters by selecting operation of the individual power converter in the vicinity of this operating point.

Future work is going to be directed towards further experimental validation and full implementation of the proposed DC bus power distribution system including the related DC/DC power converter coordination strategy on a hybrid skidder vehicle.

CRediT authorship contribution statement

Matija Krznar: Conceptualization, Methodology, Software, Investigation, Writing – original draft, Resources, Validation. **Danijel Pavković:** Methodology, Formal analysis, Visualization, Writing – review & editing, Supervision. **Mihael Cipek:** Visualization, Writing – review & editing, Supervision, Project administration, Funding acquisition.

Declaration of competing interest

The authors declare that they have no known competing financial interests or personal relationships that could have appeared to influence the work reported in this paper.

Data availability

Data will be made available on request.

Acknowledgments

It is gratefully acknowledged that this research has been supported by the European Regional Development Fund (ERDF) under the grant No. KK.01.1.1.04.0010 (HiSkid).

References

Abdallah, R.A., Shenoy, P.S., Shanbhag, N.R., Krein, P.T., 2011. System energy minimization via joint optimization of the DC-DC converter and the core. In: Proceedings of the 2011 IEEE/ACM International Symposium on Low Power Electronics and Design. Fukoka, Japan, pp. 97–102. http://dx.doi.org/10.1109/ISLPED.2011.5993614.

Beccuti, A.G., Kvasnica, M., Papafotiou, G., Morari, M., 2013. A decentralized explicit predictive control paradigm for parallelized DC-DC circuits. IEEE Trans. Control Syst. Technol. 21 (1), 136–148. http://dx.doi.org/10.1109/TCST.2011.2178071.

Cardoso, D.S., Fael, P.O., Espírito-Santo, A., 2020. A review of micro and mild hybrid systems. Energy Rep. 6, 385–390. http://dx.doi.org/10.1016/j.egyr.2019.08.077.

Cimini, G., Ippoliti, G., Orlando, G., Longhi, S., Miceli, R., 2017. A unified observer for robust sensorless control of DC–DC converters. Control Eng. Pract. 61, 21–27. http://dx.doi.org/10.1016/j.conengprac.2017.01.012.

Cipek, M., Pavković, D., Kljaić, Z., Mlinarić, T.-J., 2019. Assessment of battery-hybrid diesel-electric locomotive fuel savings and emission reduction potentials based on a realistic mountainous rail route. Energy 173, 1154–1171. http://dx.doi.org/10.1016/j.energy.2019.02.144.

Deutz, AG., 2004. D914L06 Operation Manual. Cologne, Germany, [Online]. Available: http://www.deutz.de.

2021. Droking.com. [Online]. Available: https://www.droking.com/cs/2016/02/16/dc-to-dc-buck-converter-step-down-voltage-regulator-sheet/.

Fonseca, A., Aghazadeh, F., Hoop, C., Ikuma, L., Al-Qaisi, S., 2014. Effect of noise emitted by forestry equipment on workers' hearing capacity. Int. J. Ind. Ergon. 46, 105–112. http://dx.doi.org/10.1016/j.ergon.2014.05.001.

Fuhs, A.E., 2009. Hybrid Vehicles and the Future of Personal Transportation. CRC Press, ISBN: 978-1-420-07534-2.

Gao, F., Kang, R., Yang, T., 2019. Primary and secondary control in DC microgrids: a review. J. Mod. Power Syst. Clean Energy 7 (2), 227–242. http://dx.doi.org/10.1007/s40565-018-0466-5.

2021. Genspow gmbh. [Online]. Available: https://www.gensace.de/tattu-10000mah-22-2v-25c-6s1p-lipo-battery-pack.html.

Hamar, J., Toth, A., 2009. Agent-based control of parallel dc-dc converters. In: Proceedings of the 13th European Conference on Power Electronics and Applications. Barcelona, Spain, pp. 1–10.

Hassan, T., Cheema, K.M., Mehmood, K., Tahir, A.H., Akhtar, M., 2021. Optimal control of high-power density hybrid electric vehicle charger. Energy Rep. 7, 194–207. http://dx.doi.org/10.1016/j.egyr.2020.12.021.

2021. Hittner tractors-Croatia. [Online]. Available: http://hittner.hr/tractors.

Infineon Technologies AG, 2006. IFX80471SKV – Demo Board, User's Manual. München, Germany.

Jing, J., Liu, Y.L., Wang, Y., Huang, W., 2021. Research on energy management based on SOC in P2.5 hybrid vehicles. Energy Rep. 7, 1612–1621. http://dx.doi.org/10.1016/j.egyr.2021.09.062.

Karlušić, J., Cipek, M., Pavković, Ž., Benić, J., Šušnjar, M., 2020. Benefit assessment of skidder powertrain hybridization utilizing a novel cascade optimization algorithm. Sustainability 12 (24), 15. http://dx.doi.org/10.3390/su122410396, Paper no. 10396.

Keng, C.W., 2016. Power Converters with Digital Filter Feedback Control. Academic Press, ISBN: 978-0-128-04298-4.

Knežević, .I., 2010. Reshaping of the Power Distributor of a Skidder for the Purpose of Driving All the Wheels and Winches (Master's Thesis). University of Zagreb, Zagreb, Croatia, http://repozitorij.fsb.hr/932/ (In Croatian).

Kusakaka, K., Phiri, S.F., Numbi, B.P., 2021. Optimal energy management of a hybrid diesel generator and battery supplying a RTG crane with energy recovery capability. Energy Rep. 7, 4769–4778. http://dx.doi.org/10.1016/j.egyr.2021.07.074.

Li, B., Zhao, X., Cheng, D., Zhang, S., Xu, D., 2019. Novel hybrid DC/DC converter topology for HVDC interconnections. IEEE Trans. Power Electron. 34 (6), 5131–5146. http://dx.doi.org/10.1109/TPEL.2018.2866415.

Liu, W., 2017. Hybrid Electric Vehicle System Modeling and Control, second ed. John Wiley & Sons Ltd, ISBN: 978-1-119-27932-7.

Liu, Y., Jing, J., Jie, W., Yongjian, W., Huang, W., Yu, X., 2021. Research on vehicle mode control in P2.5 hybrid system. Energy Rep. 7, 72–85. http://dx.doi.org/10.1016/j.egyr.2021.10.052.

Luo, F.L., Ye, H., 2016. Advanced DC/DC Converters. CRC Press, ISBN: 978-1-498-77490-1.

McCollum, D., Krey, V., Kolp, P., Nagai, Y., Riahi, K., 2014. Transport electrification: A key element for energy system transformation and climate stabilization. Clim. Change 123 (3–4), 651–664. http://dx.doi.org/10.1007/s10584-013-0969-z.

2021. McPower: user manual for SNT-3050 laboratory source 30V/ 50 A. [Online]. Available: https://akkuplus.de/Labornetzgeraet-McPower-SNT-3050-regelbar-0-30V-0-50A-Switchm.

Mi, C., Abdul Masrur, M., Wenzhong Gao, D., 2017. Hybrid Electric Vechiles Principles and Applications with Practical Perspectives, second ed. John Wiley and Sons, ISBN: 978-1-118-97056-0.

Moayedi, S., Davoudi, A., 2014. Distributed cooperative load sharing in parallel DC-DC converters. In: Proceedings of the 2014 IEEE Applied Power Electronics Conference and Exposition - APEC 2014, 2014. Fort Worth, TX, USA, pp. 2907–2912. http://dx.doi.org/10.1109/APEC.2014.6803717.

Montesinos-Miracle, D., Massot-Campos, M., Bergas-Jane, J., Galceran-Arellano, S., Rufer, A., 2013. Design and control of a modular multilevel DC/DC converter for regenerative applications. IEEE Trans. Power Electron. 28 (8), 3970–3979. http://dx.doi.org/10.1109/TPEL.2012.2231702.

Murakawa, Y., Sadanda, Y., Hikihara, T., 2020. Parallelization of boost and buck type DC-DC converters by individual passivity-based control. IEICE Trans. Fundam. Electron. Commun. Comput. Sci. E103.A (3), 589–595. http://dx.doi.org/10.1587/transfun.2019EAP1069.

Naslin, P., 1968. Essentials of Optimal Control. Illife Books Ltd, London, UK, ISBN: 978-0-592-01914-7.

ON Semiconductor, 2017. RURG80100-F085: 80A/1000V Ultrafast Rectifier. Data Sheet No. 20110603A.

Pavković, D., Lobrović, M., Hrgetić, M., Komljenović, V., 2014. Battery current and voltage control system design with charging application. In: Proceedings of 2014 IEEE Multi-Conference on Systems and Control (IEEE MSC 2014). Antibes, France, pp. 1133–1138. http://dx.doi.org/10.1109/CCA.2014.6981481.

Pavković, D., Lobrović, M., Hrgetić, .A., 2016a. A design of cascade control system and adaptive load compensator for battery/ultracapacitor hybrid energy storage-based direct current microgrid. Energy Convers. Manage. 114, 154–167. http://dx.doi.org/10.1016/j.enconman.2016.02.005.

Pavković, D., Sedić, A., Guzović, Z., 2016b. Oil drilling rig diesel power-plant fuel efficiency improvement potentials through rule-based generator scheduling and utilization of battery energy storage system. Energy Convers. Manage. 121, 194–211. http://dx.doi.org/10.1016/j.enconman.2016.05.022.

Potočnik, I., Poje, A., 2017. Forestry ergonomics and occupational safety in high ranking scientific journals from 2005–2016. Croat. J. For. Eng. 38 (2), 291–310.

Saber, A.Y., Venayagamoorthy, G.K., 2011. Plug-in vehicles and renewable energy sources for cost and emission reductions. IEEE Trans. Ind. Electron. 58 (4), 1229–1238. http://dx.doi.org/10.1109/TIE.2010.2047828.

Sarvi, M., Derakhshan, M., Sedighizadeh, M., 2014. A new intelligent controller for parallel DC/DC converters. Int. J. Eng. 27 (1), 131–142. http://dx.doi.org/10.5829/idosi.ije.2014.27.01a.16.

Schön, A., Bakran, M., 2015. Comparison of the most efficient DC-dc converters for power conversion in HVDC grids. In: Proceedings of PCIM Europe 2015; International Exhibition and Conference for Power Electronics, Intelligent Motion, Renewable Energy and Energy Management. Nuremberg, Germany, pp. 1–9.

Schröder, D., 2007. Elektrische Antriebe – Regelung Von Antriebssystemen, third ed. Springer-Verlag, Berlin, Germany, ISBN: 978-3-642-30096-7.

Sorrell, S., Speirs, J., Bentley, R., Brandt, A., Miller, R., 2010. Global oil depletion: A review of the evidence. Energy Policy 38 (9), 5290–5295.

Wang, R., 2020. Multi-objective configuration optimization method for a diesel-based hybrid energy system. Energy Rep. 6, 2146–2152. http://dx.doi.org/10.1016/j.egyr.2020.08.004.

Wang, Y., Biswas, A., Rodriguez, R., Keshavarz-Motamed, Z., Emadi, A., 2022. Hybrid electric vehicle specific engines: State-of-the-art review. Energy Rep. 8, 832–852. http://dx.doi.org/10.1016/j.egyr.2021.11.265.

Williamson, S.S., Emadi, A., Rajashekara, K., 2007. Comprehensive efficiency modeling of electric traction motor drives for hybrid electric vehicle propulsion applications. IEEE Trans. Veh. Technol. 56 (4), 1561–1572. http://dx.doi.org/10.1109/TVT.2007.896967.

Yilmaz, M., Krein, P.T., 2013. Review of battery charger topologies, charging power levels, and infrastructure for plug-in electric and hybrid vehicles. IEEE Trans. Power Electron. 28 (5), 2151–2169. http://dx.doi.org/10.1109/TPEL.2012.2212917.

Yong, J.Y., Ramachandramurty, V.K., Tan, K.M., Mithulananthan, N., 2015. A review of the state-of-the-art technologies of electric vehicle, its impacts and prospects. Renew. Sustain. Energy Rev. 49, 365–385. http://dx.doi.org/10.1016/j.rser.2015.04.130.

Zhong, Q.-C., Hornik, T., 2013. Control of Power Inverters in Renewable Energy and Smart Grid Integration. John Wiley & Sons Ltd/IEEE Press, NY, USA.